ADVANCED ELECTRONIC MATERIALS
www.advelectronicmat.de

A Spin–Orbit-Torque Memristive Device

*Shuai Zhang, Shijiang Luo, Nuo Xu, Qiming Zou, Min Song, Jijun Yun, Qiang Luo, Zhe Guo, Ruofan Li, Weicheng Tian, Xin Li, Hengan Zhou, Huiming Chen, Yue Zhang, Xiaofei Yang, Wanjun Jiang, Ka Shen, Jeongmin Hong, Zhe Yuan, Li Xi, Ke Xia, Sayeef Salahuddin, Bernard Dieny, and Long You**

Memristors, demonstrated by solid-state devices with continuously tunable resistance, have emerged as a new paradigm for self-adaptive networks that require synapse-like functions (artificial synapse, for example). Spin-based memristors offer advantages over other types of memristors because of their significant endurance and high energy efficiency. Yet it remains a challenge to build dense and functional spintronic memristors with structures and materials that are compatible with existing ferromagnetic devices. Here, a memristive device based upon Ta/CoFeB/MgO heterostructures is demonstrated, which are commonly used in out-of-plane magnetized magnetic tunnel junctions (MTJ). To achieve the memristive function, a domain wall (DW) is driven back and forth in a continuous manner in the CoFeB layer by applying in-plane positive or negative current pulses along the Ta layer, utilizing the spin–orbit torque (SOT) that the current exerts on the CoFeB magnetization. Hence, the magnetization and consequently the anomalous Hall effect (AHE) resistance are modulated in an analog manner, being controlled by the pulsed current characteristics including amplitude, duration, and repetition number. The quasi-continuous AHE resistance variation is explained by the SOT-induced DW creep motion. These results pave the way for developing SOT-based energy-efficient neuromorphic systems.

Memristors, demonstrated by solid-state devices with continuously tunable resistance,[1–7] have emerged as a new paradigm for self-adaptive networks that require synapse-like functions (artificial synapse, for example). Spin-based memristors offer advantages over other types of memristors because of their significant endurance and high energy efficiency.[8,9] Yet, it remains a challenge to build dense and functional spintronic memristors with structures and materials that are compatible with existing ferromagnetic devices.[10] Here, a memristive device based upon Ta/CoFeB/MgO heterostructures is demonstrated, which are commonly used in out-of-plane magnetized magnetic tunnel junctions.[11] To achieve the memristive function, a domain wall (DW) is driven back and forth in a continuous manner in the CoFeB layer by applying in-plane positive or negative current pulses along the Ta layer, utilizing the spin–orbit torque (SOT) that the current exerts on the CoFeB magnetization.[12–17] Hence,

S. Zhang, S. Luo, Q. Luo, Dr. Z. Guo, R. Li, W. Tian, X. Li, H. Chen, Prof. Y. Zhang, Prof. X. Yang, Prof. J. Hong, Prof. L. You
School of Optical and Electronic Information
Huazhong University of Science and Technology
Wuhan 430074, China
E-mail: lyou@hust.edu.cn

Dr. N. Xu, Prof. S. Salahuddin
Department of Electrical Engineering and Computer Sciences
University of California
Berkeley, CA 94720, USA

Q. Zou
Department of Electrical and Computer Engineering
University of Nebraska-Lincoln
Lincoln, NE 68588-0511, USA

Dr. M. Song
Faculty of Physics and Electronic Science
Hubei University
Wuhan 430062, China

The ORCID identification number(s) for the author(s) of this article can be found under https://doi.org/10.1002/aelm.201800782.

DOI: 10.1002/aelm.201800782

J. Yun, Prof. L. Xi
Key Laboratory for Magnetism and Magnetic Materials
of Ministry of Education
Lanzhou University
Lanzhou 730000, China

Dr. H. Zhou, Prof. W. Jiang
Department of Physics
Tsinghua University
Beijing 100084, China

Prof. K. Shen, Prof. Z. Yuan, Prof. K. Xia
The Center for Advanced Quantum Studies and Department of Physics
Beijing Normal University
100875 Beijing, China

Prof. B. Dieny
Université Grenoble Alpes
CEA
CNRS
Grenoble INP
INAC-Spintec
38000 Grenoble, France

Prof. L. You
Wuhan National Lab for Optoelectronics
Huazhong University of Science and Technology
Wuhan 430074, China

the magnetization, and consequently the anomalous Hall effect (AHE) resistance, is modulated in an analog manner, being controlled by the pulsed current characteristics including amplitude, duration, and repetition number. The quasi-continuous AHE resistance variation is explained by the SOT-induced DW creep motion. These results pave the way for developing SOT-based energy-efficient neuromorphic systems.

Spintronic memristors are resistive switching devices in which the resistance can be varied in an analog and non-volatile manner between a minimum and a maximum resistance depending on the charge that have traversed the device. They can be based on tunnel magnetoresistance (TMR) or anomalous Hall effect (AHE) resistance.[8] So far, a few studies have experimentally reported spintronic memristors based on domain wall (DW) manipulation, through spin transfer torque (STT).[9,10] However, only a few discrete resistance states were observed in these experiments, due to the fact that DW can only be pinned at a few locations. Spin–orbit torque (SOT), generated by current injection in heavy metal (HM)/ferromagnet (FM) bilayers, has attracted great attention as an alternative method to switch the magnetization[14,15] and to move DW[18] or magnetic skyrmion[19] in an FM layer, instead of or cooperating with magnetic field, STT, and electric field.[20–23] Very recently, Fukami et al. demonstrated analog memristive behavior induced by SOT in a PtMn/[Co/Ni] antiferromagnetic (AFM)/FM bilayer system by performing R–I sweeps.[16] The memristive switching mechanism in this system was theoretically considered to be predominantly governed by domain nucleation instead of DW propagation, though comprehensive understanding of the mechanism was not clear. According to the experiments and explanation in ref. [16], the resistance of these devices may remain constant when repetitive current pulses with a fixed amplitude and duration are applied. Such behavior is not desirable for the realization of synaptic plasticity since the memristor resistance should be changeable in an analog manner by the number of applied pulses.[4,5]

In this paper, we report SOT-induced memristive behavior in Ta/CoFeB/MgO heterostructures. These structures are commonly used in interfacial PMA-based magnetic tunnel junctions (MTJs) which exhibit large TMR and are implemented in commercial magnetic RAM (MRAM) products.[11,24] The electrical measurements show that the AHE resistance of our devices can be tuned continuously by current pulses. In addition, the magnetic domain structure was investigated by magneto-optic Kerr effect (MOKE) microscopy. These characterizations confirmed that the observed continuous resistance change is associated with DW propagation in creep regime.

Our deposited film stack comprises the following layers: thermally oxidized Si substrate/Ta (10 nm)/CoFeB (1.2 nm)/MgO (1.6 nm)/Ta (20 nm) (see Experimental Section). The stack is patterned into 50×400 μm^2 Hall bar structures. To evaluate the perpendicular component of the magnetization, the Hall resistance (R_H) due to the AHE is measured. The structure of the stack and measurement setup are shown in **Figure 1**a. The AHE loop (R_H vs out-of-plane field H_z) confirms the strong PMA of the CoFeB magnet with a coercivity field, H_c, of 10 Oe and an anisotropy field, H_k, of 4000 Oe (see Supporting Information S1). Next, we investigate the response of R_H to the in-plane current (I) under

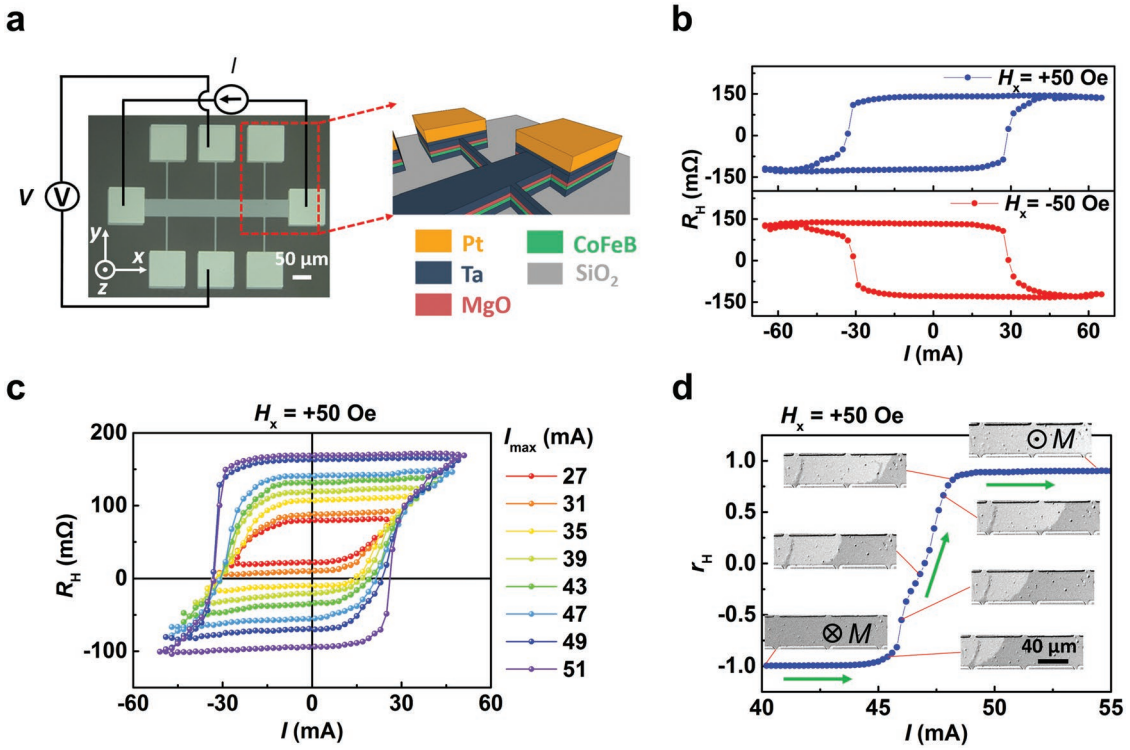

Figure 1. SOT memristor based on Ta/CoFeB/MgO heterostructures. a) Device structure with schematic of the measurement setup. b) Current-induced switching under a small constant magnetic field $H_x = \pm 50$ Oe. c) R_H–I loops with varying maximum current magnitude, I_{max}, under $H_x = +50$ Oe. d) Normalized resistance r_H as a function of current pulses (0.1 ms pulse width) accompanied by the real-time MOKE images of Hall bars.

a small in-plane field, $H_x = \pm 50$ Oe (see Experimental Section), as shown in Figure 1b. At $H_x = +50$ Oe, the current generates hysteretic magnetic switching between upward ($M\uparrow$, $R_H > 0$) and downward ($M\downarrow$, $R_H < 0$) polarization states, and the positive current (along $+x$ direction) favors $M\uparrow$ (blue curve). When the small constant field H_x is reversed, the current-driven transitions are inverted, and positive current now favors $M\downarrow$ (red curve). Such bipolar switching behavior is a signature of SOT generation at the Ta/CoFeB interface due to spin Hall effect and at the CoFeB/MgO interface due to Rashba effect.[14,15] Furthermore, the reversal of the R_H is not abrupt; rather it looks like a continuous transition with numerous intermediate resistance values (from –0.1 to 0.15 Ω, here). If one varies the maximal magnitude of the current, I_{max}, from low (27 mA) to high (51 mA), a series of hysteretic loops are observed, as depicted in Figure 1c, indicating that the final resistance state can effectively be determined by the current cycle protocol. At the maximum current magnitude used (50 mA), the device temperature can increase up to 380 K (Supporting Information S2). However, since the direction of magnetization switching depends on the polarity of the current, it cannot be attributed to Joule heating.

To provide insight into the magnetization dynamics associated with the change in resistance, MOKE microscopy was performed on the Hall bars, as shown in Figure 1d. To obtain a clearer observation, the Ta capping layer of the device was thinned by etching. Starting from a saturated state $M\downarrow$ corresponding to the normalized resistance value $r_H = -1$, the application of consecutive positive current pulses nucleates a reversed domain at the left edge of the strip, followed by propagation of the DW and the correlated continuous variation of the resistance. An almost saturated state $M\uparrow$ ($r_H = +1$) is eventually reached as the in-plane current is large enough. These MOKE images clearly indicate that the memristive behavior in our HM/FM bilayer system originates from DW propagation. In addition, by applying the field at various angles θ with respect to the normal to the sample and looking at the variation of the switching field H_{SW}, it was found that the variation $H_{SW}(\theta)$ follows a $1/\cos\theta$ law which, according to the Kondorsky model,[25] suggests that DW motion dominates the magnetization switching (see details in Supporting Information S3).

If a train of current pulses with alternating polarity is applied in conjunction with the collinear in-plane field (**Figure 2**a), a gradual resistance modulation can be observed, provided that the pulse amplitude exceeds the bipolar switching activation threshold, I_{th}, of the device (as illustrated in Figure 2b). The resistance value starts at approximately 0 Ω, corresponding to a demagnetized state. Thus, the I_{th} required for current-driven DW motion by SOT is expected to be the same for both polarities ($I_{th} = \pm 46$ mA, here). R_H depends not only on the pulse-train amplitude but also on the pulse duration and number of repetitions. Figure 2c–f presents the pulse duration/number phase diagrams for different pulse amplitudes (see Experimental Section). The results show that the quasi-continuous resistance gradually decreases (increases)

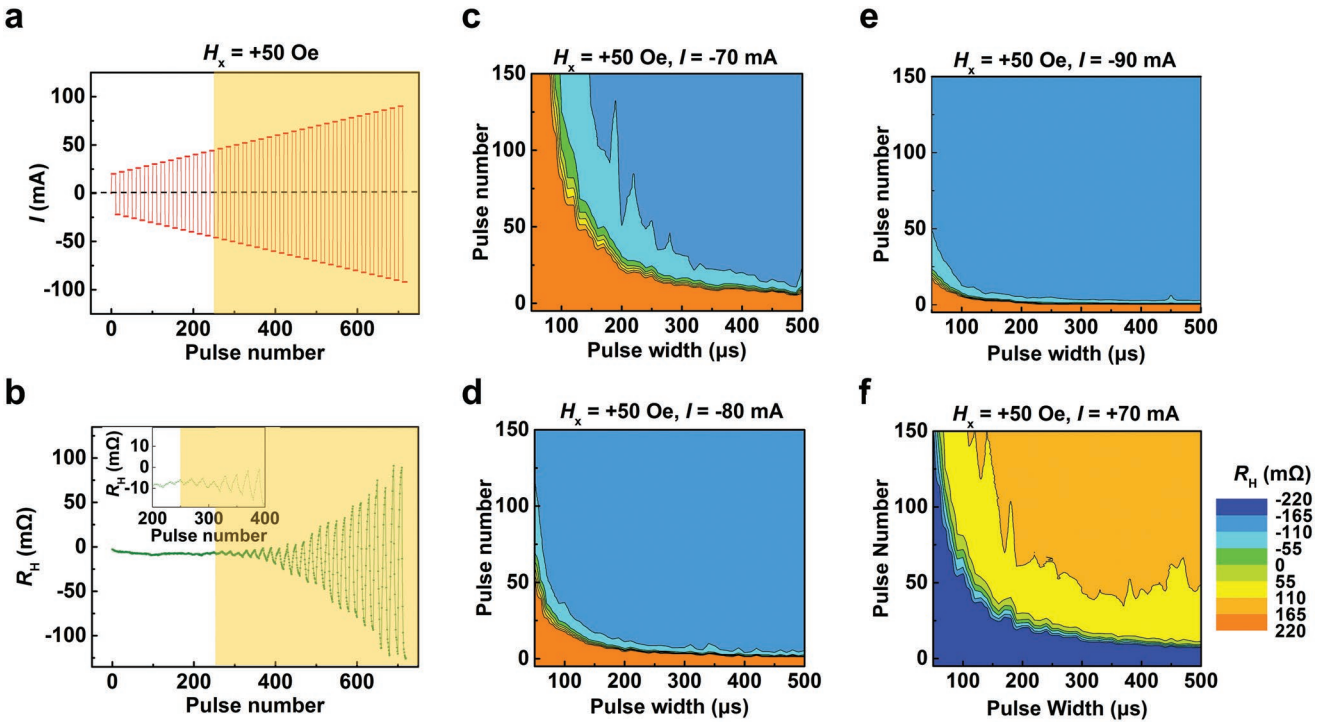

Figure 2. Tuning R_H using amplitude, polarity, duration, and number of consecutive current pulses. a) Current modulation applied to the sample corresponding to a sequence of pulses 50 μs long of alternating polarity and increasing amplitude. b) Resistance modulation resulting from the sequence of pulses described in (a). Current thresholds to observe resistance changes are found for both polarities ($I_{th} = \pm 46$ mA) and indicated by the yellow shaded areas. The inset in (b) shows a zoomed-in image of the change in resistance around the threshold region. c–f) Phase diagrams of R_H as a function of the pulse width and pulse number for four pulse amplitudes c) $I = -70$ mA, d) –80 mA, e) –90 mA, and f) +70 mA under an in-plane field $H_x = +50$ Oe.

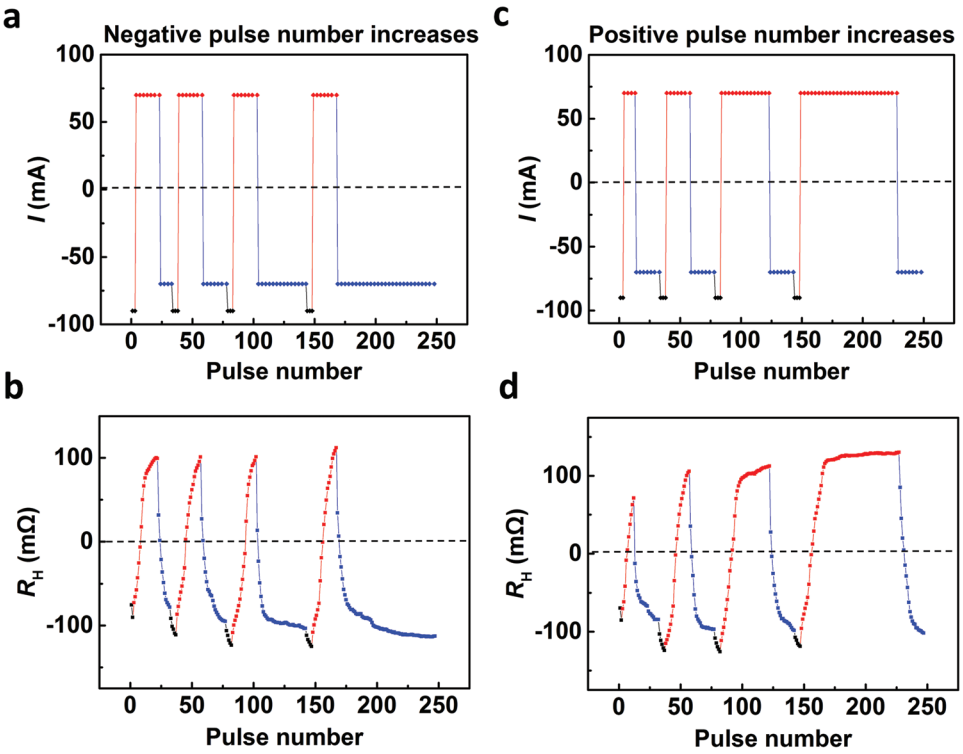

Figure 3. Resistance tuning obtained by programming consecutive pulse sequences (duration in 150 µs) under $H_x = +50$ Oe. a) Current-pulse sequence applied to the sample characterized by sequences of positive pulses of fixed number alternating with sequences of negative pulses of increasing number. b) AHE resistance responses to the current excitation of (a). c) Current-pulse sequence applied to the sample characterized by sequences of positive pulses of increasing number alternating with sequences of negative pulses of fixed number. d) AHE resistance responses to the current excitation of (c). The magnetization was initially saturated in the downward state by a reset pulse of −90 mA. The pulse amplitudes are +70 and −70 mA for positive and negative values, respectively.

with the number of consecutive pulses, which is caused by continuous downward (upward) magnetic switching modulated by the pulses (see details in Supporting Information S4). Such a cumulative effect further validates the memristive functionality of our device. We note that R_H varies more abruptly with a longer duration and/or higher amplitude of pulse (Figure 2c–e), which correlates with the DW motion depending on the pulse duration/amplitude.

In particular, the resistance variation induced by programming consecutive pulses sequences can be utilized to imitate synaptic behaviors,[26] such as "long-term potentiation and depression" (LTPD).[4,5] This is illustrated in **Figure 3**. We first saturate the magnetization in the $M_\downarrow$ state by a reset pulse (−90 mA). Next, we apply positive pulses with a fixed amplitude (+70 mA) and number of pulses (20) and subsequently negative pulses with a constant amplitude (−70 mA) but an increasing number of pulses (from 10 to 20, 40, and 80), as shown in Figure 3a. The response of R_H to these consecutive pulses sequences (see Figure 3b) indicates that positive pulses with the same properties (such as amplitude, duration, and number) can reproducibly determine the same resistance state (0.1 Ω), whereas the change in number of negative pulses enables different resistance levels. Similarly, R_H gradually increases when the number of positive pulses varies (from 10 to 20, 40, and 80 successively; see Figure 3c,d). As a result, the behavior of the resistance variation shown in Figure 3a,b illustrates the long-term depression effects, while the trend in Figure 3c,d illustrates the long-term potentiation effects. The synaptic plasticity (LTPD) further demonstrates that our memristive device can be used in self-adaptive networks with synaptic functionality. Note that there is an asymmetry behavior in synaptic potentiation and depression process, which might originate from the difference of DW velocity under positive and negative pulses. To improve the symmetry, the amplitudes of applied positive and negative pulses could be set to different value. Besides, a nonlinearity behavior of R_H versus pulse number is observed when R_H approaches saturation value. Therefore, it is better for the SOT memristive device to work in quasi-linear region, with a smaller amplitude or shorter pulse width adopted to tune the resistance more controllably.

In memristive devices, a common approach to continuously modulating the resistance is to apply consecutive identical pulses.[4–6] **Figure 4**a–d shows the evolution of r_H and the corresponding magnetization dynamics as a function of cumulative pulse time (t). Under positive pulses, the state is gradually set to $r_H = +1$, while under negative pulses, it gradually reaches $r_H = -1$. Three key stages emerge during the evolution of the magnetization switching. As depicted in Figure 4a (b), segment B–C (B′–C′) represents the memristive stage, where r_H gradually increases (decreases) with the pulse time due to DW motion in the AHE detection region. When the DWs have not yet reached or have already left the detection region, r_H remains

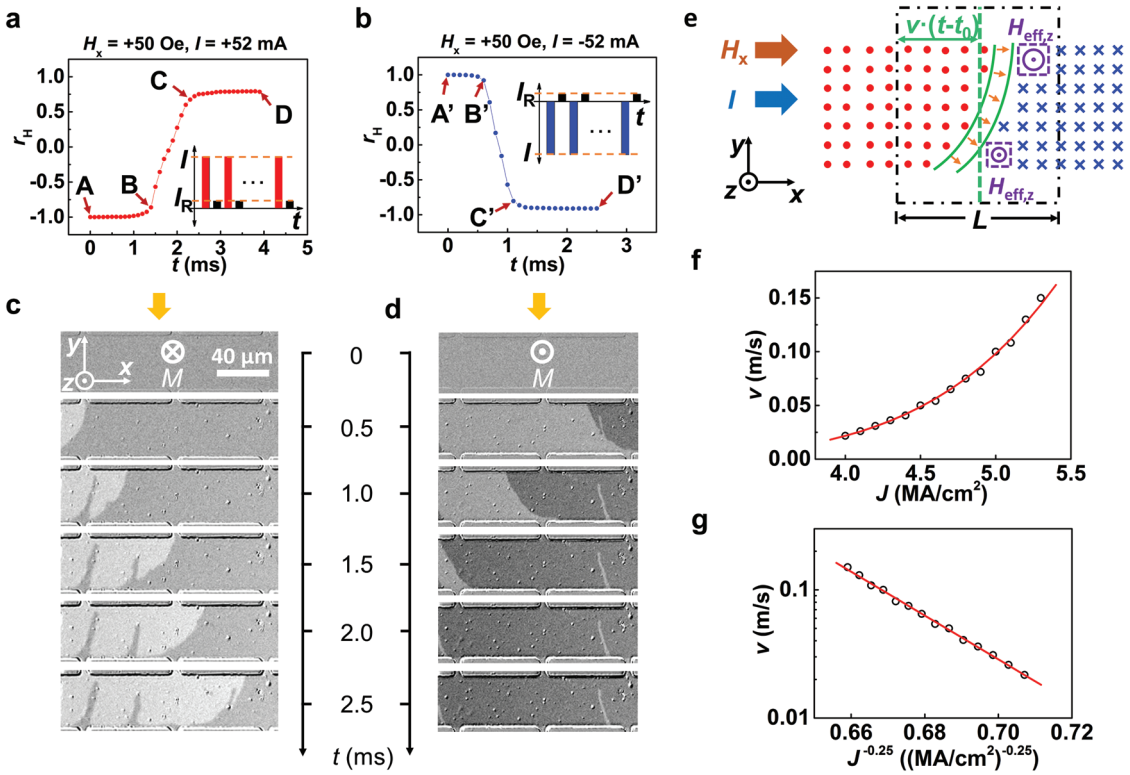

Figure 4. Resistance and magnetization switching dynamics. a–d) Dependence of the a,b) resistive state and the c,d) corresponding magnetization dynamics on the cumulative pulse time (t) for a,c) down-to-up and b,d) up-to-down switching. A small in-plane field of +50 Oe is applied. e) Schematic of the magnetic moment orientation near the DW with right-handed chirality. The black dashed frame represents the region where AHE resistance is measured. The tilted DW is equalized to a straight line (green dotted line). f) DW velocity, v, versus current density J. g) Scaling plot of log v versus $J^{-0.25}$.

constant, as shown in A–B and C–D in Figure 4a (A′–B′ and C′–D′ in Figure 4b).

The MOKE images further reveal that these DWs are actually right-handed chiral Néel walls stabilized by Dzyaloshinskii–Moriya interaction (DMI)[27,28] since the observed direction of the DW motion is always the same as that of the current flow (see Figure 4c,d; Figure S6, Supporting Information). The DMI effective field (H_{DMI}) in our system is estimated to be approximately 100 Oe (see Supporting Information S6). The schematic in Figure 4e describes the magnetization reversal by DW propagation (the case in Figure 4c). The orientation of the SOT effective field ($H_{eff,z}$) acting on the Néel walls is aligned with the magnetization of one of the adjacent domains.[29] Therefore, the DW can move along the current flow direction until the whole CoFeB magnetization has been switched. We can conclude that the memristive switching behavior in the Ta/CoFeB/MgO structure is induced by SOT-driven Néel-type DW motion. In addition, the DMI leads to a tilting of the DWs during their motion.[30] The vertical component of the Oersted field is found to have opposite polarity at the two long edges of the device (see details in Supporting Information S7) and might also contribute to the observed tilting.

Moreover, we find that the extracted velocity (v) of DW motion in this work is slow compared to that (10–100 m s^{-1}) in previous reports.[31] For example, the velocity shown in Figure 4c,d is estimated to be approximately 0.1 m s^{-1} (see Supporting Information S8). Due to this low velocity, the continuous variation of R_H and the memristive behavior can clearly be observed instead of abrupt bipolar switching. To investigate this further, we study the behavior of v as a function of the current density (J) under an in-plane field of 50 Oe (see details in Supporting Information S8), as shown in Figure 4f. The observed nonlinear dependence of v on J may result from the motion in the creep regime[32] and follows the universal Arrhenius scaling relation[33]:

$$\log(v) \propto J^{-\mu} \tag{1}$$

where μ is the creep exponent, found to be ≈0.25 for field-driven creep both in Pt/Co/Pt and Ta/CoFeB/MgO systems.[32,34–36] Here, SOT can be treated as an effective field as mentioned above, so we assume that μ = 0.25. Figure 4g shows the plot of log-scale v as a function of $J^{-0.25}$. The good correlation between them confirms that the DW motion is well described by Equation (1) and the creep model.

The comparison of the electrical measurements with the MOKE images (Figure 4a–d) shows that the resistance varies systematically with the relative fraction of the upward domains, s. This trend can be well reproduced using a simple model that considers r_H to vary linearly with s. During resistance modulation dynamics, s varies from 0 (1) at the onset of switching to 1 (0) for down-to-up (up-to-down) reversal in the detection region. Following the assumptions above, one can write

$$r_H = 2s - 1, 0 \le s \le 1. \quad (2)$$

The evolution of s is roughly proportional to t and v and can be expressed as

$$s = v \times (t - t_0)/L, t \ge t_0 \quad (3)$$

for down-to-up switching and as

$$s = 1 - v \times (t - t_0)/L, t \ge t_0 \quad (4)$$

for up-to-down switching, where L is the length of the detection region (see Figure 4e) and t_0 is the intrinsic propagation time when the DW reaches the detection region.

Thus, Equations (1)–(4) impose a strict framework for resistance response as a function of external electrical excitation. In other words, R_H can be a function of I and t ($R_H = R(I, t)$) for our devices to imitate a memristor. For practical applications, our Ta/CoFeB/MgO heterostructures can be implemented as the free-layer stack in MTJs, in which a larger TMR will be obtained. Moving from the AHE measurement to practical application in MTJs, the evolution of s (the relative fraction of the upward domains) will result in an immediate response in the TMR variation without an intrinsic propagation time, i.e., $t_0 = 0$ in Equations (3) and (4). To further optimize the device structure, one of the approaches to realize field-free SOT switching of PMA materials could be used for our SOT memristors, namely either by introducing a lateral structural asymmetry,[37] engineering a tilted anisotropy,[38] or using interlayer exchange coupling.[39] Furthermore, the relative proportion of upward- and downward-polarized magnetic domains can be controlled by SOT at nanometer scale,[40] which enables SOT-memristor applications in high-density and low-power artificial neural networks.

In conclusion, we have reported memristive behavior in a Ta/CoFeB/MgO multilayered structure, which is commonly used in STT magnetic random access memory. The resistance can be effectively tuned by current pulses, whose amplitude, polarity, duration, and number can be varied. We established a connection between the memristive behavior and SOT-induced magnetization dynamics by deriving an understanding of the underlying mesoscopic switching mechanisms. Slowly propagating DWs generate a creep in the detection area of the device, which yields a broad range of intermediate resistive states in the AHE measurements. The Ta/CoFeB/MgO memristor device offers a practical structure that relies on mature magnetic-material technology. As such, it could pave the way towards the integration of high-density, energy-efficient components for non-volatile storage and neuromorphic computing applications.

Experimental Section

Sample Preparation: A thin-film stack of Ta (10 nm)/CoFeB (1.2 nm)/MgO (1.6 nm)/Ta (20 nm) was sputter-deposited on a thermally oxidized Si substrate at room temperature without a post-annealing process. Vibrating sample magnetometer was used to characterize the magnetic properties of the thin-film stack and ensure that it exhibited perpendicular magnetic anisotropy (Supporting Information S1). Hall bars were fabricated by photolithography and argon-ion milling. A Ta (10 nm)/Pt (100 nm) bilayer was capped on pads as electrodes by photolithography and lift-off techniques. The width and length of the channel in the Hall devices were 50 and 400 μm, respectively; those of the Hall probes were 5 and 100 μm, respectively.

Electrical Measurements: For the anomalous Hall resistance (R_H) measurement, a constant 0.1 mA bias read current (I_R) was applied using a DC current source (Keithley Model 6221), and the Hall voltage (V_R) was measured using a nanovoltmeter (Keithley Model 2182A) in the usual way. The same current source was used to apply current pulses (I) for the current-induced switching and the phase-diagram measurements. A unipolar current pulse with a duration of 0.5 s was used for the current-induced switching in Figure 1b,c. In particular, in Figure 1c, first, the FM was set into a demagnetization state ($R_H = 0\ \Omega$) excited by a DC current (60 mA) in the absence of a magnetic field and then the magnitude was increased from the current cycles to maximum (from 27 to 51 mA). In the switching phase-diagram measurements, the pulse width was varied from 50 to 500 μs in increments of 10 μs. Before each measurement, the magnet was initialized to a saturated state $M_\uparrow$ (Figure 2c–e) or $M_\downarrow$ (Figure 2f). The initial intermediate state corresponding to $R_H = 0\ \Omega$ in Figure 2b was also excited by a DC current (60 mA) in the absence of a magnetic field.

Magneto-Optic Kerr Effect Imaging: A MOKE microscope was used to magnetically image the Hall bars. To observe contrast, first, the magnet was saturated in the $-z$ or $+z$ direction, and an image was taken. This served as a reference image. Next, a current pulse with a width of 0.1 ms under an in-plane field was applied, and another image was taken. Finally, the two images were aligned, and the first reference image was subtracted from the second image to generate the final MOKE image, which was used in this work.

Supporting Information

Supporting Information is available from the Wiley Online Library or from the author.

Acknowledgements

The authors acknowledge the financial support from the National Natural Science Foundation of China (NSFC Grant No. 61674062).

Conflict of Interest

The authors declare no conflict of interest.

Keywords

artificial synapses, domain walls, memristors, spin–orbit torque

Received: November 3, 2018
Revised: December 6, 2018
Published online: January 30, 2019

[1] L. Chua, *IEEE Trans. Circuit Theory* **1971**, *18*, 507.
[2] D. B. Strukov, G. S. Snider, D. R. Stewart, R. S. Williams, *Nature* **2008**, *453*, 80.
[3] J. J. Yang, M. D. Pickett, X. Li, D. A. Ohlberg, D. R. Stewart, R. S. Williams, *Nat. Nanotechnol.* **2008**, *3*, 429.

[4] S. H. Jo, T. Chang, B. B. Bhadviya, P. Mazumder, W. Lu, *Nano Lett.* **2010**, *10*, 1297.
[5] T. Chang, S. H. Jo, K. H. Kim, P. Sheridan, S. Gaba, W. Lu, *Appl. Phys. A* **2011**, *102*, 857.
[6] A. Chanthbouala, V. Garcia, R. O. Cherifi, K. Bouzehouane, S. Fusil, X. Moya, S. Xavier, H. Yamada, C. Deranlot, N. D. Mathur, M. Bibes, A. Barthélémy, J. Grollier, *Nat. Mater.* **2012**, *11*, 860.
[7] B. K. You, W. I. Park, J. M. Kim, K.-I. Park, H. K. Seo, J. Y. Lee, Y. S. Jung, K. J. Lee, *ACS Nano* **2014**, *8*, 9492.
[8] X. Wang, Y. Chen, H. Xi, H. Li, D. Dimitrov, *IEEE Electron Device Lett.* **2009**, *30*, 294.
[9] A. Chanthbouala, R. Matsumoto, J. Grollier, V. Cros, A. Anane, A. Fert, A. V. Khvalkovskiy, K. A. Zvezdin, K. Nishimura, Y. Nagamine, H. Maehara, K. Tsunekawa, A. Fukushima, S. Yuasa. *Nat. Phys.* **2011**, *7*, 626.
[10] S. Lequeux, J. Sampaio, V. Cros, K. Yakushiji, A. Fukushima, R. Matsumoto, H. Kubota, S. Yuasa, J. Grollier, *Sci. Rep.* **2016**, *6*, 31510.
[11] S. Ikeda, K. Miura, H. Yamamoto, K. Mizunuma, H. D. Gan, M. Endo, S. Kanai, J. Hayakawa, F. Matsukura, H. Ohno, *Nat. Mater.* **2010**, *9*, 721.
[12] M. I. Dyakonov, V. I. Perel, *Phys. Lett. A* **1971**, *35*, 459.
[13] J. E. Hirsch, *Phys. Rev. Lett.* **1999**, *83*, 1834.
[14] I. M. Miron, K. Garello, G. Gaudin, P.-J. Zermatten, M. V. Costache, S. Auffret, S. Bandiera, B. Rodmacq, A. Schuhl, P. Gambardella, *Nature* **2011**, *476*, 189.
[15] L. Liu, C.-F. Pai, Y. Li, H. W. Tseng, D. C. Ralph, R. A. Buhrman, *Science* **2012**, *336*, 555.
[16] S. Fukami, C. Zhang, S. DuttaGupta, A. Kurenkov, H. Ohno, *Nat. Mater.* **2016**, *15*, 535.
[17] K. Cai, M. Yang, H. S. Wang, Y. Ji, B. Li, K. W. Edmonds, Y. Sheng, B. Zhang, N. Zhang, S. Liu, H. Zheng, K. Wang, *Nat. Mater.* **2017**, *16*, 712.
[18] J. M. Lee, K. Cai, G. Yang, Y. Liu, R. Ramaswamy, P. He, H. Yang, *Nano Lett.* **2018**, *18*, 4669.
[19] S. Luo, M. Song, X. Li, Y. Zhang, J. Hong, X. Yang, X. Zou, N. Xu, L. You, *Nano Lett.* **2018**, *18*, 1180.
[20] N. Sato, F. Xue, R. M. White, C. Bi, S. X. Wang, *Nat. Electron.* **2018**, *1*, 508.
[21] M. Wang, W. Cai, D. Zhu, Z. Wang, J. Kan, Z. Zhao, K. Cao, Z. Wang, Y. Zhang, T. Zhang, C. Park, J.-P. Wang, A. Fert, W. Zhao, *Nat. Electron.* **2018**, *1*, 582.
[22] Z. Wang, L. Zhang, M. Wang, Z. Wang, D. Zhu, Y. Zhang, W. Zhao, *IEEE Electron Device Lett.* **2018**, *39*, 343.
[23] S. C. Baek, K.-W. Park, D.-S. Kil, Y. Jang, J. Park, K.-J. Lee, B.-G. Park, *Nat. Electron.* **2018**, *1*, 398.
[24] M. Wang, W. Cai, K. Cao, J. Zhou, J. Wrona, S. Peng, H. Yang, J. Wei, W. Kang, Y. Zhang, J. Langer, B. Ocker, A. Fert, W. Zhao, *Nat. Commun.* **2018**, *9*, 671.
[25] E. Kondorsky, *J. Phys.* **1940**, *2*, 161.
[26] S. H. Jo, T. Chang, I. Ebong, B. B. Bhadviya, P. Mazumder, W. Lu, *Nano Lett.* **2010**, *10*, 1297.
[27] S. Emori, U. Bauer, S. M. Ahn, E. Martinez, G. S. Beach, *Nat. Mater.* **2013**, *12*, 611.
[28] G. Yu, P. Upadhyaya, K. L. Wong, W. Jiang, J. G. Alzate, J. Tang, P. K. Amiri, K. L. Wang, *Phys. Rev. B* **2014**, *89*, 104421.
[29] O. J. Lee, L. Q. Liu, C. F. Pai, Y. Li, H. W. Tseng, P. G. Gowtham, J. P. Park, D. C. Ralph, R. A. Buhrman, *Phys. Rev. B* **2014**, *89*, 024418.
[30] O. Boulle, S. Rohart, L. D. Buda-Prejbeanu, E. Jué, I. M. Miron, S. Pizzini, J. Vogel, G. Gaudin, A. Thiaville, *Phys. Rev. Lett.* **2013**, *111*, 217203.
[31] S. S. P. Parkin, M. Hayashi, L. Thomas, *Science* **2008**, *320*, 190.
[32] S. Lemerle, J. Ferré, C. Chappert, V. Mathet, T. Giamarchi, P. Le Doussal, *Phys. Rev. Lett.* **1998**, *80*, 849.
[33] P. Chauve, T. Giamarchi, P. Le Doussal, *Phys. Rev. B* **2000**, *62*, 6241.
[34] L. San Emeterio Alvarez, K.-Y. Wang, S. Lepadatu, S. Landi, S. J. Bending, C. H. Marrows, *Phys. Rev. Lett.* **2010**, *104*, 137205.
[35] J.-C. Lee, K.-J. Kim, J. Ryu, K.-W. Moon, S.-J. Yun, G.-H. Gim, K.-S. Lee, K.-H. Shin, H.-W. Lee, S.-B. Choe, *Phys. Rev. Lett.* **2011**, *107*, 067201.
[36] S. DuttaGupta, S. Fukami, C. Zhang, H. Sato, M. Yamanouchi, F. Matsukura, H. Ohno, *Nat. Phys.* **2016**, *12*, 333.
[37] G. Yu, P. Upadhyaya, Y. Fan, J. G. Alzate, W. Jiang, K. L. Wong, S. Takei, S. A. Bender, L.-T. Chang, Y. Jiang, M. Lang, J. Tang, Y. Wang, Y. Tserkovnyak, P. K. Amiri, K. L. Wang, *Nat. Nanotechnol.* **2014**, *9*, 548.
[38] L. You, O. J. Lee, D. Bhowmik, D. Labanowski, J. Hong, J. Bokor, S. Salahuddin, *Proc. Natl. Acad. Sci. U. S. A.* **2015**, *112*, 10310.
[39] Y.-C. Lau, D. Betto, K. Rode, J. M. D. Coey, P. Stamenov, *Nat. Nanotechnol.* **2016**, *11*, 758.
[40] M. Baumgartner, K. Garello, J. Mendil, C. O. Avci, E. Grimaldi, C. Murer, J. Feng, M. Gabureac, C. Stamm, Y. Acremann, S. Finizio, S. Wintz, J. Raabe, P. Gambardella, *Nat. Nanotechnol.* **2017**, *12*, 980.